

# Alternate Synthesis Method for High-Performance Manganese Rich Cation Disordered Rocksalt Cathodes

Shripad Patil, Devendrasinh Darbar, Ethan C. Self,\* Thomas Malkowski, Vincent C. Wu, Raynald Giovine, Nathan J. Szymanski, Rebecca D. McAuliffe, Bo Jiang, Jong K. Keum, Krishna P. Koirala, Bin Ouyang, Katharine Page, Chongmin Wang, Gerbrand Ceder, Raphaële J. Clément, and Jagjit Nanda\*

Cation-disordered rocksalt (DRX) cathodes have recently emerged as a promising class of cobalt-free, high-capacity cathodes for lithium-ion batteries. To facilitate their commercialization, the development of scalable synthesis techniques providing control over composition and morphology is critical. To this end, a sol-gel synthesis route to prepare Mn-rich DRX cathodes with high capacities is presented here. Several compositions with varied Mn content and nominal F doping are successfully prepared using this technique. In-situ X-ray diffraction measurements demonstrate that DRX formation proceeds at moderate temperature (800 °C) through the sol-gel route, which enables intimate mixing among reactive intermediate phases that form at lower temperatures. All synthesized compositions possess cation short-range order, as evidenced by neutron pair distribution function and electron diffraction analysis. These DRX materials demonstrate promising electrochemical performance with reversible capacities up to 275 mAh g. Compared to the baseline oxide ( $\text{Li}_{1.2}\text{Mn}_{0.4}\text{Ti}_{0.4}\text{O}_2$ ), the Mn-rich compositions exhibit improved cycling stability, with some showing an increase in capacity upon cycling. Overall, this study demonstrates the feasibility of preparing high-capacity DRX cathodes through a sol-gel based synthesis route, which may be further optimized to provide better control over the product morphology compared to traditional synthesis methods.

## 1. Introduction

The past few decades of research and development have produced highly optimized lithium-ion batteries (LIBs) for applications such as electric vehicles and grid storage.<sup>[1]</sup> To further improve these technologies and accelerate the transition to clean energy, new electrode materials with increased energy density, better safety, and reduced cost are needed. At present, these factors are primarily limited by the cathode active material. Layered intercalation cathodes such as  $\text{LiCoO}_2$  (LCO) and  $\text{LiNi}_x\text{Mn}_y\text{Co}_{1-x-y}\text{O}_2$  (NMC) currently dominate the LIB market as they provide high specific energy (e.g.,  $\approx 700\text{--}800\text{ Wh kg}^{-1}$  for Ni-rich NMC) and excellent cycling stability.<sup>[2–5]</sup> Despite the promising performance of LCO and NMC cathodes, the high Ni and Co content in these cathodes leads to high costs and poses a threat to supply chain stability.<sup>[6,7]</sup> Hence, the development of Co/Ni-free cathodes is critical to meet ever-growing energy demands.

S. Patil  
Bredesen Center for Interdisciplinary Research and Education  
University of Tennessee Knoxville  
Knoxville, TN 37966, USA

S. Patil, D. Darbar, E. C. Self, T. Malkowski, R. D. McAuliffe, J. Nanda<sup>[†]</sup>  
Chemical Sciences Division  
Oak Ridge National Laboratory  
Oak Ridge, TN 37830, USA  
E-mail: selfec@ornl.gov; jnanda@slac.stanford.edu

V. C. Wu, R. Giovine, R. J. Clément  
Materials Department  
UC Santa Barbara  
Santa Barbara, CA 93106, USA

V. C. Wu, R. Giovine, R. J. Clément  
Materials Research Laboratory  
UC Santa Barbara  
Santa Barbara, CA 93106, USA

 The ORCID identification number(s) for the author(s) of this article can be found under <https://doi.org/10.1002/aenm.202203207>.

<sup>[†]</sup>Present address: Applied Energy Division, SLAC National Laboratory, 2575 Sand Hill Road, Menlo Park CA 94025, USA

DOI: 10.1002/aenm.202203207

N. J. Szymanski, B. Ouyang, G. Ceder  
Department of Material Science & Engineering  
UC Berkeley  
Berkeley, CA 94720, USA

N. J. Szymanski, B. Ouyang, G. Ceder  
Materials Science Division  
Lawrence Berkeley National Laboratory  
Berkeley, CA 94720, USA

B. Jiang, J. K. Keum, K. Page  
Neutron Scattering Division  
Oak Ridge National Laboratory  
Oak Ridge, TN 37831, USA

J. K. Keum  
Center for Nanophase Materials Sciences  
Oak Ridge National Laboratory  
Oak Ridge, TN 37831, USA

K. P. Koirala  
Physical and Computational Sciences Directorate  
Pacific Northwest National Laboratory  
Richland, WA 99354, USA

Lithium-excess cation disordered rocksalt (DRX) materials have emerged as a promising class of cathodes that can achieve high specific energy (up to 1000 Wh kg<sup>-1</sup>) and utilize low-cost, earth-abundant elements such as Mn and Ti.<sup>[8–11]</sup> In contrast to the well-ordered crystal structures of traditional Li-ion cathodes (e.g., layered, spinel, and olivine cathodes), DRX materials are characterized by a high level of disorder within the cation sublattice, where facile lithium transport is enabled by percolating Li-rich clusters.<sup>[8,9]</sup> The high capacity of DRX cathodes is attributed to a combination of transition metal and oxygen redox processes.<sup>[12–15]</sup> Increasing the redox-active transition metal content, in addition to partial fluorine substitution for oxygen, reduces the reliance on oxygen redox and improves the cycling stability of DRX cathodes.<sup>[12,16–26]</sup> However, it remains challenging to synthesize DRX compositions with high fluorine content (>10%) using synthesis techniques that are scalable and can provide control over the particle morphology, warranting the exploration of alternate synthesis strategies.<sup>[27]</sup>

DRX cathodes are typically synthesized via high temperature solid-state routes.<sup>[17,18,20,28,29]</sup> Although such routes often result in the desired DRX phase, they require that precursor powders are well mixed through mechanical mixing/milling to ensure a fast and homogenous reaction upon heating, and they provide poor control over particle morphology. Additionally, DRX oxyfluorides prepared by such methods are limited by the fluorine solubility in the rocksalt oxide framework. Using first-principle calculations, Ouyang et al. found that Mn<sup>3+</sup>/Ti<sup>4+</sup>-based DRX compositions have low fluorine solubility and can only substitute 5.7% of the anion sites at 1000 °C, and related compositions generally have comparably low fluorine solubility (e.g., <10% of anion sites at 1000 °C).<sup>[17]</sup> In addition to solid-state routes, high-energy mechanochemical methods have been used to successfully synthesize DRX oxyfluorides such as Li<sub>2</sub>Mn<sub>1/2</sub>Ti<sub>1/2</sub>O<sub>2</sub>F,<sup>[12,21,25,30]</sup> though such methods are difficult to scale, provide little control over particle size and morphology, and often yield materials with poor crystallinity. Alternate synthesis routes are therefore desirable to produce DRX cathodes in a scalable and controllable fashion.

In this work, a sol-gel-based synthesis route was developed to prepare Mn/Ti-based DRX cathodes. Compared to traditional solid-state and mechanochemical routes, sol-gel methods enable homogenous, atomic-scale mixing of the precursors,<sup>[31]</sup> which can lead to lower energy reaction pathways and facilitate the formation of the desired phase during annealing. Sol-gel processes can also produce powders with controlled morphology at relatively low temperatures while maintaining excellent control over product purity and homogeneity. Because of these advantages, sol-gel synthesis has previously been explored for various other LIB cathode materials.<sup>[32–36]</sup> Here we target several DRX cathodes with nominal compositions Li<sub>1.2</sub>Mn<sub>0.4</sub>Ti<sub>0.4</sub>O<sub>2</sub>, Li<sub>1.2</sub>Mn<sub>0.5</sub>Ti<sub>0.3</sub>O<sub>1.9</sub>F<sub>0.1</sub>, Li<sub>1.2</sub>Mn<sub>0.6</sub>Ti<sub>0.2</sub>O<sub>1.8</sub>F<sub>0.2</sub>, and Li<sub>1.2</sub>Mn<sub>0.7</sub>Ti<sub>0.1</sub>O<sub>1.7</sub>F<sub>0.3</sub>,

hereafter referred to as LMTO04, LMTOF05, LMTOF06, and LMTOF07, respectively based on the Mn content (LMTOF samples). With X-ray diffraction (XRD), we confirm that all samples are composed of a single DRX phase, with no detectable crystalline impurities. However, energy dispersive X-ray spectroscopy (EDX) and solid-state nuclear magnetic resonance (ssNMR) spectroscopy measurements reveal that the fluorinated samples have lower-than-expected F contents (0.1 – 0.6 at%), likely due to LiF volatilization during heating.<sup>[27]</sup> Despite their low F contents, they show promising electrochemical performance with capacities up to ≈275 mAh g<sup>-1</sup> and improved capacity retention after 50 cycles compared to the baseline oxide. Notably, some Mn-rich compositions exhibit an increase in discharge capacity with cycling, which warrants further investigations into the redox mechanisms of these materials.

## 2. Results and Discussion

### 2.1. Sol-Gel Synthesis

The pure DRX oxide phase (LMTO04) was prepared using a sol-gel synthesis procedure outlined schematically in **Figure 1**, which highlights two key experimental steps: (i) a sol-gel reaction to produce an intermediate oxide precursor followed by (ii) high-temperature calcination. In the sol-gel step, metal

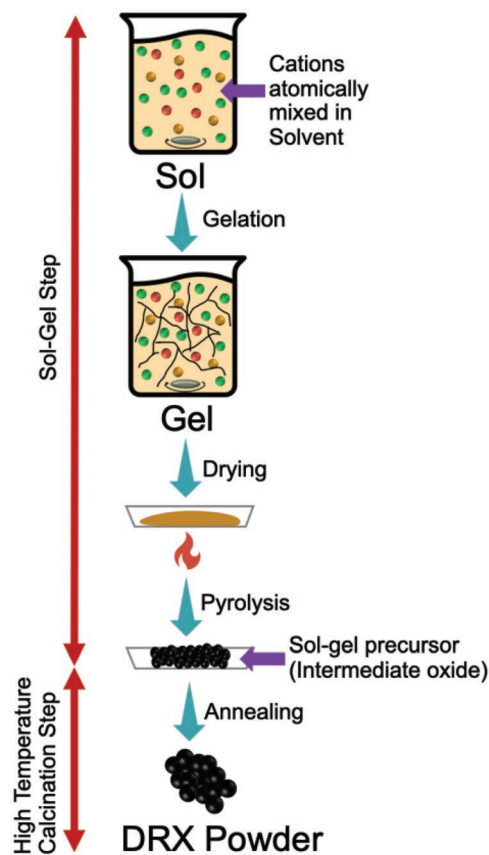


**Figure 1.** A schematic of the sol-gel synthesis procedure used for the preparation of DRX cathodes in this work.

K. Page  
Department of Material Science & Engineering  
University of Tennessee Knoxville  
Knoxville, TN 37966, USA

C. Wang  
Environmental Molecular Sciences Laboratory  
Pacific Northwest National Laboratory  
Richland, WA 99354, USA

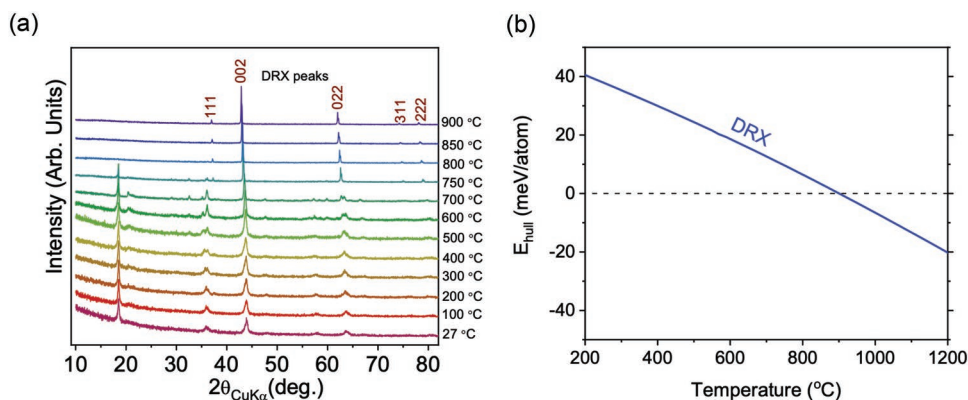


**Figure 2.** a) In-situ XRD used to study the phase evolution of the sol-gel precursor for LMTO04. The hkl peaks at 900 °C represent the DRX phase b) Calculated energy above the hull ( $E_{\text{hull}}$ ) associated with LMTO04, determined using ab-initio cluster expansion calculations.

precursors (manganese acetate tetrahydrate, lithium nitrate, and titanium isopropoxide) dissolved in ethanol undergo hydrolysis and polycondensation reactions as the solvent is evaporated to form a network of atomically mixed cations (gelation).<sup>[31]</sup> The dried gel was pyrolyzed at 400 °C to produce an intermediate oxide mixture, which was then subjected to high-temperature calcination to obtain the desired DRX phase. Additional details on the synthesis procedure are provided in the Experimental Section.

Phase evolution of the sol-gel precursor during calcination of LMTO04 was evaluated using in situ XRD as shown in **Figure 2(a)**. The sample initially contained a mixture of  $\text{LiMn}_2\text{O}_4$  (spinel) and  $\text{Li}_2\text{TiO}_3$  (monoclinic) formed during the pyrolysis of the gel at 400 °C (Figure S1, Supporting Information shows the XRD pattern of the sol-gel precursor). Although the precursors were prepared with a nominal 1:1 cation:anion ratio to produce a DRX phase, we suspect that oxidation occurred during pyrolysis (performed in air), thereby forming the anion-rich spinel phase (cation-anion ratio of 3:4). Moreover, our ab-initio calculations reveal that LMTO04 is only metastable at 400 °C, lying 30 meV/atom above the convex hull. The calculated energy above hull ( $E_{\text{hull}}$ ), as defined with respect to all competing phases in the Li-Mn-Ti-O space, is plotted for the DRX phase as a function of temperature in **Figure 2(b)**. This plot reveals that LMTO04 only becomes stable above 900 °C owing to increased entropic contributions from configurational disorder in the cation sublattice. High temperature stabilization of the disordered configuration is confirmed by the in-situ XRD measurements displayed in **Figure 2(a)**, which show that a DRX phase forms above 800 °C, in addition to a minor  $\text{Mn}_3\text{O}_4$  impurity phase that reacts upon further heating. For comparison, LMTO04 was also synthesized using a conventional solid-state route, which was characterized using in situ XRD (Figure S2, Supporting Information). In contrast to the sol-gel approach, solid-state synthesis required annealing at higher temperatures ( $\geq 900$  °C) for longer times ( $>9$  hours) to obtain phase-pure LMTO04. The improved reaction rate achieved using a sol-gel approach is attributed to more intimate mixing between the precursors, thus providing an efficient alternative to more energy-intensive techniques such as ball milling.

Ex situ XRD and  $^7\text{Li}$  ssNMR characterization on sol-gel samples annealed at 750 °C, 900 °C, and 1000 °C for 1 h were

performed to identify the optimal annealing temperature, as presented in **Figure 3**. While XRD is sensitive to crystalline phases,  $^7\text{Li}$  ssNMR probes the local environments of Li nuclei in amorphous and crystalline phases and can easily distinguish ordered/disordered paramagnetic phases (here, Mn-containing, and redox active) from diamagnetic impurities in DRX samples. Li nuclei in (possibly amorphous) diamagnetic impurities result in sharp  $^7\text{Li}$  signals centered  $\approx 0$  ppm. On the other hand, the chemical shift of Li nuclei present in the cathode structure is dominated by paramagnetic interactions between the Li spins and unpaired  $d$  electron spins arising from  $\text{Mn}^{3+}$  species, resulting in a broad NMR line shape and a large Fermi contact shift. The magnitude and direction of this shift depend on both the number of  $\text{Mn}^{3+}$  ions in close proximity ( $<5$  Å) to Li and on the Li-O-Mn bond angle. In the disordered rocksalt structure,  $\text{Li}^+$  has: (i) 12 nearest-neighbor metal (M) ions ( $\text{M} = \text{Li}^+, \text{Mn}^{3+}$ , or  $\text{Ti}^{4+}$ ) connected through a  $90^\circ$  Li-O-M bond angle and (ii) 6 next-nearest-neighbor M ions connected through a  $180^\circ$  Li-O-M bond angle. Hence, for a sufficiently disordered system, the presence of a large number of different Li environments results in a very broad spectrum with limited spectral resolution.<sup>[37]</sup> In contrast, the ordering of the metals on the cation sites, as in spinel or layered rocksalt oxides, significantly reduces the number of distinct Li environments, resulting in discrete  $^7\text{Li}$  ssNMR resonances.

As the reaction temperature is increased from 750 °C to 1000 °C, cation-ordered phases stabilized at lower temperatures evolve into a cation-disordered phase, as demonstrated by both XRD and  $^7\text{Li}$  ssNMR. At 750 °C, a mixture of layered oxide (spinel, monoclinic), DRX, and trace  $\text{Mn}_3\text{O}_4$  phases were observed from the XRD patterns shown in **Figure 3(a)**. Similarly, the corresponding  $^7\text{Li}$  ssNMR spectrum contains many sharp signals characteristic of Mn-based ordered oxide structures in line with the XRD results as shown in **Figure 3(b)**. Upon increasing the temperature to 900 °C, XRD indicates the sample was predominantly DRX with a minor ordered impurity phase (small peak at  $2\theta = 18^\circ$ ). These findings are supported by the  $^7\text{Li}$  ssNMR spectrum obtained on the same sample, which exhibits: (i) sharp signals characteristic of ordered phases, albeit with significantly reduced intensity than that of the 750 °C sample and (ii) a broad underlying asymmetric signal indicating the presence of many distinct Li local environments, as is expected for

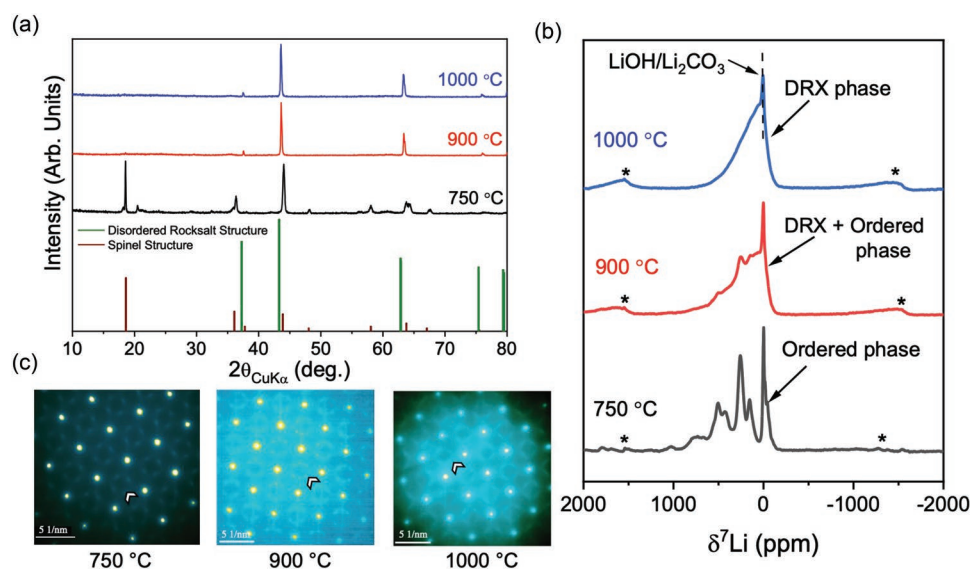


**Figure 3.** The phase evolution of LMTO04 DRX samples annealed at 750 °C, 900 °C, and 1000 °C for 1 h. At each temperature, the products are characterized by: a) XRD, b)  $^7\text{Li}$  ssNMR, and c) electron diffraction. Asterisks in panel (b) indicate spinning sidebands due to the fast rotation of the sample during ssNMR data acquisition. Arrows in panel (c) are used to highlight diffuse scattering patterns that arise due to SRO in the cation sublattice of the DRX phase.

the DRX phase. A phase-pure LMTO04 DRX without any crystalline ordered impurities is formed at 1000 °C as confirmed by XRD. The presence of a dominant broad and asymmetric line-shape in the  $^7\text{Li}$  ssNMR spectrum and the absence of notable sharp signals (other than a low-intensity resonance at 0 ppm, corresponding to (an) amorphous impurity phase(s) such as Li<sub>2</sub>CO<sub>3</sub> or LiOH often present in DRX synthesis products) confirms the formation of a mostly phase pure DRX.

The ex situ XRD and ssNMR results indicate that heating above 900 °C for a short duration is desirable to obtain a pure DRX phase when using the sol-gel synthesis route presented here. This finding agrees well with our ab-initio calculations, which suggest that the desired DRX phase is thermodynamically stable only at temperatures above 900 °C (Figure 2(b)). Additionally, electron diffraction patterns were collected on the 750 °C, 900 °C, and 1000 °C samples as shown in Figure 3(c). These patterns contain: (i) bright Bragg spots associated with a DRX structure and (ii) diffuse scattering patterns suggesting cation short-range ordering (SRO) in these samples.

## 2.2. Materials Characterization

The sol-gel-based route was extended to prepare Mn-rich DRX oxyfluorides (LMTOF05, LMTOF06, and LMTOF07). In this process, the pyrolyzed sol-gel precursor was mechanically milled with LiF and annealed at 1000 °C. As shown in Figure 4(a), XRD patterns from the as-synthesized LMTO04, LMTOF05, LMTOF06, and LMTOF07 DRX samples confirm the formation of a DRX structure (spacegroup  $Fm\bar{3}m$ ) with no significant crystalline impurities.

Neutron total scattering data was collected to probe the long-range and local structure of these materials. Rietveld refinements were performed on the neutron diffraction data assuming a structure model with a random cation distribution

(Figure S3, Supporting Information). This analysis indicates a monotonic increase in the cubic lattice parameter with increasing manganese content, from 4.1489 Å for LMTO04 to 4.1647 Å for LMTOF07 (Figure S4, Supporting Information) which reflects the incorporation of larger Mn<sup>3+</sup> ions (64.5 pm vs 60.5 for Ti<sup>4+</sup> ions) into the lattice. Figure 4(b) shows the neutron pair distribution function (N-PDF) analysis performed on the total scattering data to study the local structure of these LMTOF samples. Previous studies have shown that SRO in DRX cathodes has a dramatic influence on their electrochemical properties, especially their rate capability.<sup>[17,38–43]</sup> Based on the refinements performed here, a random cation distribution model provides a reasonable fit of the experimental data for long-range features; however, this model is unable to capture many of the subtle short-range (<6 Å) features (e.g., peak splitting). The SRO evidenced by N-PDF is consistent with the observed diffuse scattering in electron diffraction patterns collected on the same set of samples (Figure S5, Supporting Information). A more detailed analysis of the nature of the SRO using advanced modeling methods (e.g., Reverse Monte Carlo simulations) will be the focus of a future study.

Scanning electron microscopy (SEM) was used to examine the particle morphology in the as-synthesized LMTOF DRX samples. These samples contain irregularly shaped particles with sizes ranging from sub-micron to 20 μm, as shown in Figure S6 (Supporting Information). Sample compositions were evaluated using scanning transmission electron microscope – energy dispersive X-ray spectroscopy (STEM-EDX) mapping, inductively coupled plasma–optical emission spectroscopy (ICP-OES), and fluoride-ion selective electrode (F-ISE) measurements. Figure 4(c) shows that all LMTOF samples contain a homogenous distribution of Mn, Ti, O, and F. Elemental compositions, as determined by EDX mapping are summarized in Table S1 (Supporting Information). The measured Mn/Ti ratio is consistent with the nominal composition; however,

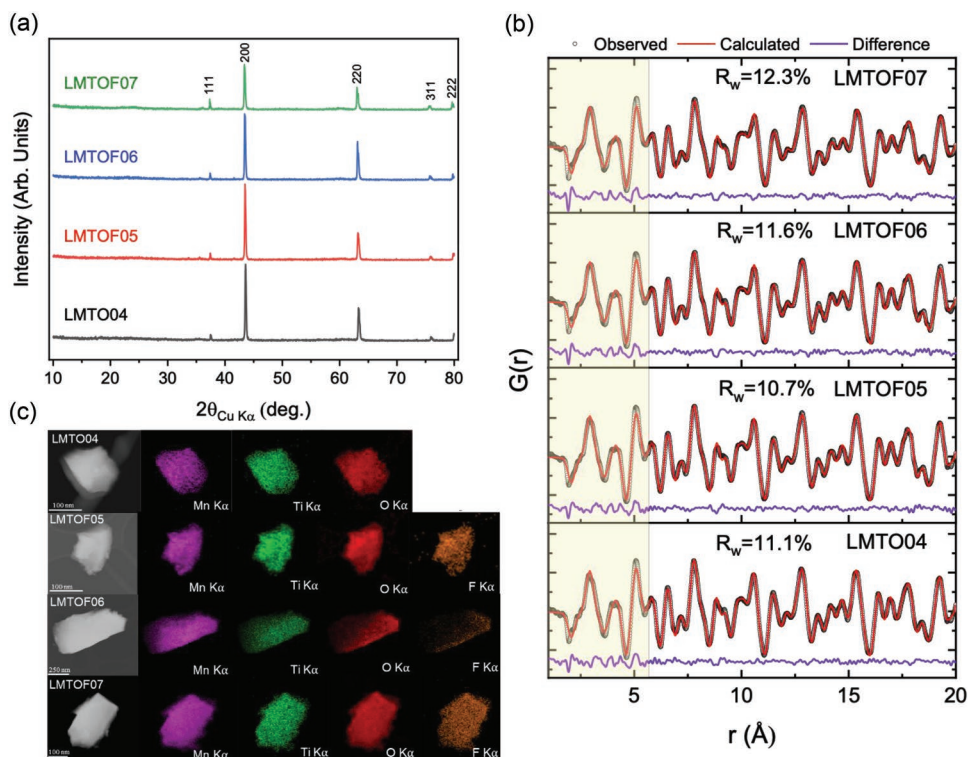


**Figure 4.** a) XRD patterns of as-synthesized LMTO04, LMTOF05, LMTOF06, and LMTOF07. All samples were indexed to the cubic rocksalt phase ( $Fm\bar{3}m$ ), b) Neutron pair distribution function analysis of LMTO04, LMTOF05, LMTOF06, and LMTOF07. The refinement was performed using a structural model with a random cation distribution within the cation sublattice, c) Morphology and elemental distribution of particles in LMTOF DRX samples. STEM-HAADF images and EDX maps are shown for LMTO04, LMTOF05, LMTOF06, and LMTOF07.

the measured O/F ratio is higher than the targeted value, indicating a lower-than-expected fluorine content. For example, LMTOF05 has an O/F ratio of 32 compared to the nominal value of 19. This finding is supported by the elemental compositions obtained from ICP-OES and F-ISE indicating that the LMTOF05, LMTOF0.6, and LMTOF0.7 samples only contain 0.14, 0.59, and 0.59 at% F, respectively, compared to the target values of 2.5, 5, and 7.5 at% (Table S2, Supporting Information).

$^{19}\text{F}$  ssNMR was used to further assess the incorporation of fluorine (or lack thereof) into the bulk DRX structure and to differentiate it from fluorine present in diamagnetic impurities. The  $^{19}\text{F}$  ssNMR spectra of the LMTOF samples shown in Figure 5(a),(b) feature (i) a broad and asymmetric signal (from 200 ppm to  $-500$  ppm), characteristic of fluorine nuclei in paramagnetic environments and (ii) a sharp signal  $\approx -204$  ppm, attributed to a LiF diamagnetic impurity, as has been discussed in prior studies on DRX oxyfluorides.<sup>[12,18,21,25,30,40]</sup> The parameters used to record the  $^{19}\text{F}$  ssNMR spectra in Figure 5(a) were optimized (e.g., long inter-scan delay of 30 s) to ensure that all the visible  $^{19}\text{F}$  diamagnetic and paramagnetic signals are fully relaxed. It is worth noting that even under these optimized experimental conditions, the  $^{19}\text{F}$  ssNMR signals from F nuclei directly bonded to paramagnetic Mn ions are too broad and too short-lived to be observed,<sup>[40]</sup> and the observed paramagnetic to diamagnetic signals intensity ratios are only semi-quantitative. For all the samples, a low signal-to-noise ratio (SNR) is obtained despite the extensive signal averaging (512 transients collected over 4 h), which indicates the presence of only trace

amounts of F. Additionally, for LMTOF06 and LMTOF07, the intense LiF peak ( $\approx -204$  ppm) indicates that a significant fraction of the F content is present as an amorphous LiF phase and is not incorporated into the DRX structure. To better assess the evolution of the  $^{19}\text{F}$  local environments in the bulk DRX structure as the Mn content is increased across the  $\text{Li}_{1.2}\text{Mn}_{0.4+x}\text{Ti}_{0.4-x}\text{O}_{2-x}\text{F}_x$  compositional series, additional  $^{19}\text{F}$  ssNMR spectra were acquired with a short, 50 ms inter-scan delay to maximize the intensity of the fast-relaxing, paramagnetic  $^{19}\text{F}$  signals, as shown in Figure 5(b). Under these conditions, the SNR is only slightly improved despite extensive signal averaging (262, 144 transients), further confirming the limited F content in these samples. A slight increase in the average  $^{19}\text{F}$  chemical shift is observed with increasing Mn content, consistent with the presence of a greater number of Mn nuclei in the vicinity of the F nuclei on average. Overall, the  $^{19}\text{F}$  NMR results confirm that the LMTOF samples have minimal fluorine incorporation into the DRX phase in line with the F-ISE data.

The low fluorine incorporation observed in each LMTOF DRX sample is likely due to the loss of the LiF precursor at high annealing temperatures. Recent work has shown that LiF is highly volatile above its melting point (848 °C) when placed under flowing Ar.<sup>[27]</sup> This conclusion is further supported by the lower-than-stoichiometric amounts of Li detected in all LMTOF samples reported here (see ICP results in Table S2, Supporting Information). Notably, fluorination levels reported here are much lower than those previously reported for comparable

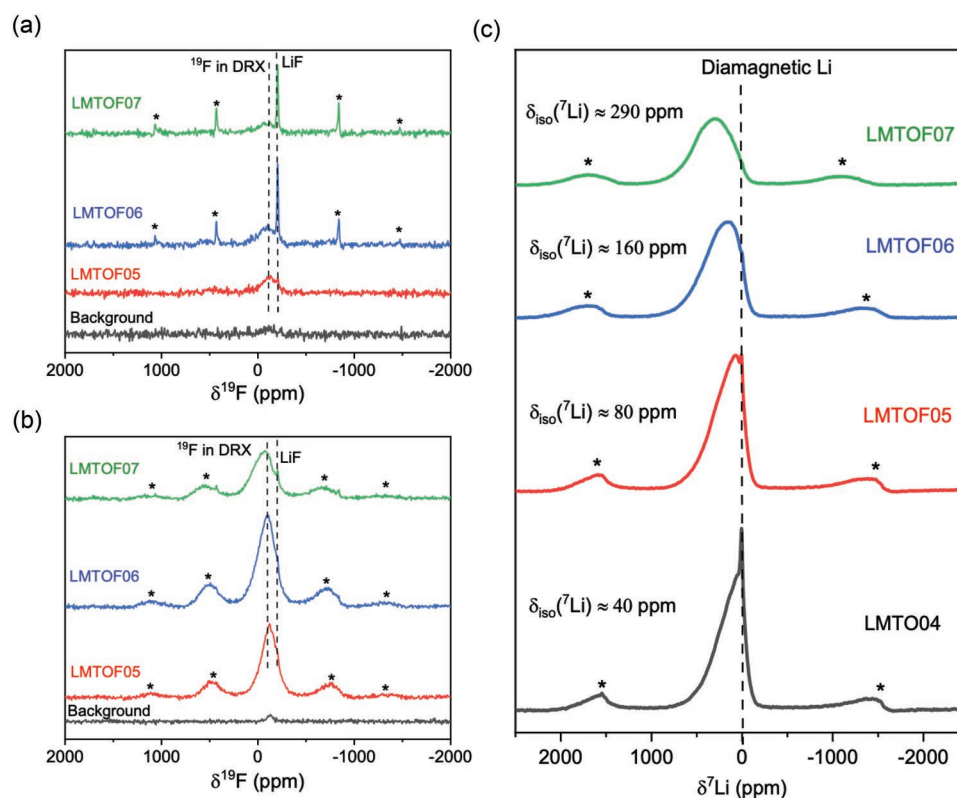


**Figure 5.** a,b)  $^{19}\text{F}$  and c)  $^7\text{Li}$  ssNMR spectra collected on LMTO04, LMTOF05, LMTOF06, and LMTOF07 samples. a)  $^{19}\text{F}$  spectra were obtained by signal averaging over 512 scans and using a long recycle delay (30 s) to ensure full relaxation of all the signals prior to excitation. b)  $^{19}\text{F}$  spectra were also recorded using a short recycle delay (50 ms) and averaged over 262, 144 transients to enhance the intensity of the fast-relaxing paramagnetic signals. c) Quantitative  $^7\text{Li}$  spectra obtained using a long recycle delay. All spectra are scaled according to the number of moles of F/Li in the rotor and the number of scans. Asterisks indicate spinning sidebands.

DRX materials synthesized using a solid-state approach (generally 2.5–5 at%).<sup>[18,21,29]</sup> This difference may be attributed to the modified reaction pathway imposed by the sol-gel method, which effectively pre-reacts the elemental precursors together before LiF is introduced. As a result, synthesis of the oxyfluoride requires that LiF react with the more stable intermediate oxide phase(s) as opposed to the precursors themselves. Such a reaction may not proceed until higher temperature, at which point LiF evaporation is likely. To resolve these issues, several different approaches for preventing LiF loss may be considered in future work including: (i) annealing the precursor mixture within a sealed ampule, (ii) more aggressive milling of LiF with the sol-gel mixture, and (iii) using alternative fluorine precursors with reduced volatility. Considering the low fluorine content of the LMTOF samples, they may be described as Mn-rich, F-doped DRX oxides.

As mentioned previously, DRX synthesis methods often result in the formation of diamagnetic Li impurities which can be observed and quantified using  $^7\text{Li}$  ssNMR. Figure 5(c) shows the  $^7\text{Li}$  spin echo NMR spectra collected on the LMTO04, LMTOF05, LMTOF06, and LMTOF07 samples, where the sharp resonance  $\approx 0$  ppm indicates the presence of diamagnetic Li-containing impurities (e.g., LiF,  $\text{Li}_2\text{O}$ ,  $\text{Li}_2\text{CO}_3$ , LiOH). These impurities are likely amorphous in nature as they were not observed in the XRD patterns, and considering their low

content, it is unlikely they have a significant impact on the DRX cathodes' electrochemical properties. Unlike  $^{19}\text{F}$  ssNMR spectra,  $^7\text{Li}$  ssNMR spectra of DRX compounds can be fully quantitative if acquired with sufficiently long inter-scan delays (Figure S7, Supporting Information). Notably, the amount of amorphous diamagnetic Li impurities ( $\approx 1$ –5%) in these samples, as obtained from fits of the overall line shape, is lower than that found in DRX materials synthesized using conventional synthesis routes (typically 10%),<sup>[12,25]</sup> suggesting that sol-gel method can lead to higher purity DRX products. We note that the amount of diamagnetic Li-containing impurities is slightly overestimated due to signal loss during the  $^7\text{Li}$  spin echo ssNMR experiment which is more severe for paramagnetic signals.

### 2.3. Electrochemical Performance

To test the electrochemical performance, composite cathodes were prepared by first milling the as-synthesized active material powders with carbon in a high-energy SPEX mill and then adding a binder solution to this mixture to prepare a slurry which was cast onto a carbon-coated aluminum current collector. The ball milling process significantly reduced the particle size of the as-synthesized material (see SEM images in

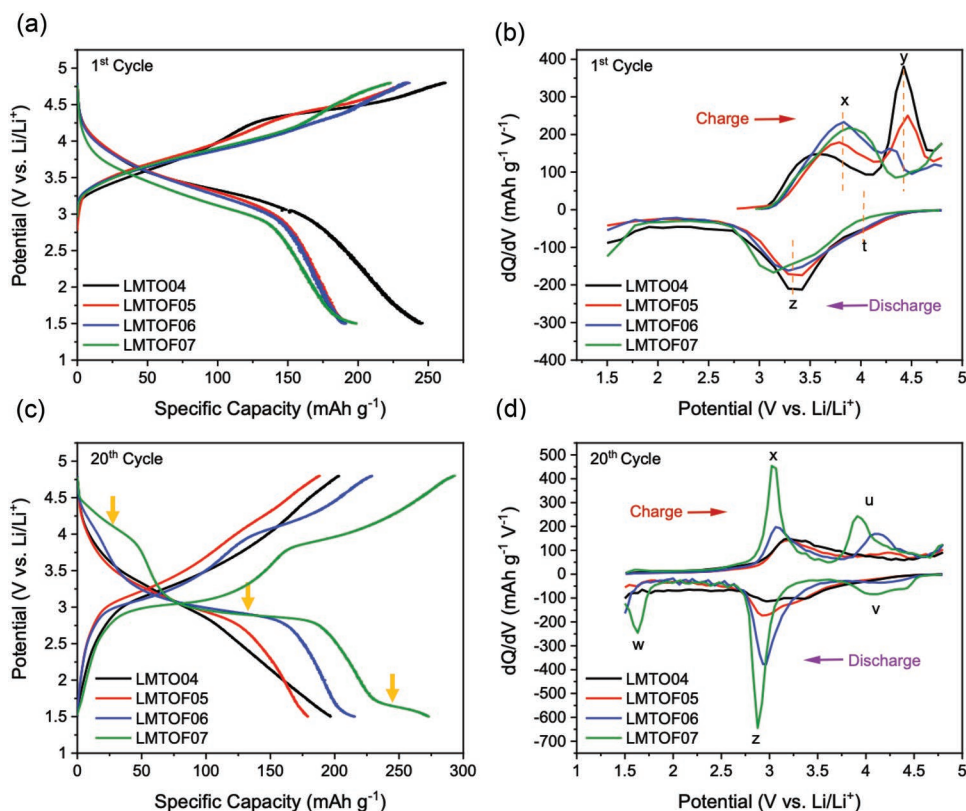


**Figure 6.** Electrochemical performance of LMT004, LMTOF05, LMTOF06, and LMTOF07 DRX half cells during (a), b) 1<sup>st</sup> cycle and (c), d) 20<sup>th</sup> cycle. (a), c) Voltage versus specific capacity plots (b), d) corresponding differential capacity versus voltage ( $dQ/dV$ ) plots. The cells were cycled between 1.5 and 4.8 V at a specific current of 10 mA  $g^{-1}$  for the 1<sup>st</sup> cycle and 20 mA  $g^{-1}$  for the 20<sup>th</sup> cycle.

Figure S8, Supporting Information) and resulted in broader XRD peaks due to a decrease in crystallite size (Figure S8, Supporting Information). **Figure 6** shows the voltage profiles and differential capacity ( $dQ/dV$ ) plots of the LMTOF cathodes cycled in half cells against Li metal anodes. The cells were cycled between 1.5 V and 4.8 V at a specific current of 10 mA  $g^{-1}$  for the first 5 cycles, and 20 mA  $g^{-1}$  for subsequent cycles. All cells exhibit a sloping charge/discharge profile during the first cycle. The first cycle charge capacities of LMT004, LMTOF05, LMTOF06, and LMTOF07 are 262 mAh  $g^{-1}$ , 235 mAh  $g^{-1}$ , 234 mAh  $g^{-1}$ , and 223 mAh  $g^{-1}$  respectively, which are higher than the capacity theoretically achievable from  $Mn^{3+}/Mn^{4+}$  redox. For comparison, the theoretical capacities from  $Mn^{3+}/Mn^{4+}$  redox calculated using the actual compositions obtained from ICP and F-ISE analysis in LMT004, LMTOF05, LMTOF06, and LMTOF07 are 131 mAh  $g^{-1}$ , 158 mAh  $g^{-1}$ , 184 mAh  $g^{-1}$ , and 201 mAh  $g^{-1}$ , respectively. As demonstrated in prior work, additional capacity beyond  $Mn^{3+}/Mn^{4+}$  redox is largely attributed to the oxygen redox process,<sup>[18,22,26,44,45]</sup> since  $Ti^{4+}$  acts only as a structural stabilizer and is electrochemically inactive over the voltage range used here.<sup>[10,46]</sup> As shown in Figure 6(b), the first cycle  $dQ/dV$  plots exhibit two peaks  $\approx 3.7$  V and 4.4 V (denoted as x and y respectively) during charging, which are related to  $Mn^{3+}/Mn^{4+}$  and oxygen oxidation processes, respectively.<sup>[18,20,22,26,44,45]</sup> For the LMTOF cathodes, the capacity from

$Mn^{3+}/Mn^{4+}$  charge compensation increases with increasing Mn content, as evidenced by the growth of peak x and the decrease of peak y. A sharp peak at 4.4 V is observed during charging for LMT004, indicating substantial oxygen redox, whereas this peak is almost nonexistent in LMTOF07. These findings support past work, wherein increasing the redox-active transition metal content has been shown to limit anionic charge compensation.<sup>[12,16–26]</sup> The first cycle discharge capacities of LMTOF05, LMTOF06, and LMTOF07 are similar (190 mAh  $g^{-1}$ , 191 mAh  $g^{-1}$ , and 199 mAh  $g^{-1}$  respectively), but substantially lower than that of LMT004 (241 mAh  $g^{-1}$ ). This discrepancy is likely due to LMT004 having a higher effective Li content compared to LMTOF05, LMTOF06, and LMTOF07 (Table S2, Supporting Information), due to LiF loss during the preparation of LMTOF samples as previously discussed. Additionally, suppression of the oxygen redox process with increasing manganese content could also play a role in lower first-cycle discharge capacities in Mn-rich compositions. During the first discharge, the  $dQ/dV$  peak  $\approx 3.3$  V is attributed to  $Mn^{4+}/Mn^{3+}$  reduction (denoted as z), and the oxygen reduction peaks (broad peaks denoted as t) have a much lower intensity compared to oxygen oxidation peaks (peak y during charge), highlighting the largely irreversible nature of the anionic charge compensation process. The first cycle coulombic efficiencies of LMT004, LMTOF05, LMTOF06, and LMTOF07 are 92.3%, 81.1%, 81.3%, and 89.1%, respectively. In general,

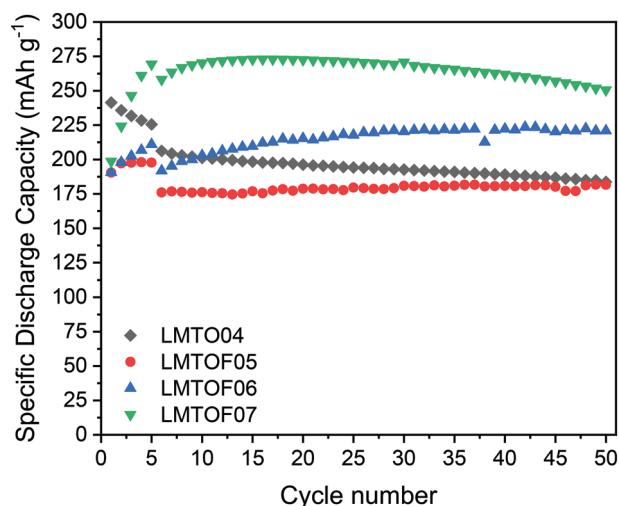


**Figure 7.** Comparison of the discharge capacity of LMTO04, LMTOF05, LMTOF06, and LMTOF07 DRX half cells during the first 50 charge-discharge cycles. The cells were cycled between 1.5 and 4.8 V at a specific current of 10 mA g<sup>-1</sup> for the first 5 cycles and 20 mA g<sup>-1</sup> for subsequent cycles.

the coulombic efficiency during cycling decreases with increasing Mn content as shown in Figure S9 (Supporting Information).

After 20 cycles, Mn-rich compositions LMTOF06 and LMTOF07 develop distinct voltage plateaus at 4, 2.7, and 1.7 V during discharge (denoted by arrows in Figure 6(c)). These changes are also evident in the corresponding dQ/dV plots shown in Figure 6(d), through the development of new peaks (denoted u, v, and w) and a shift in the Mn redox peaks to more negative values as compared to the first cycle. The evolution of the voltage profiles suggests potential structural rearrangements in LMTOF06 and LMTOF07 upon extended cycling. One possible explanation is the formation of a spinel-like phase upon extended cycling as was recently reported for other Mn-based DRX cathodes.<sup>[22,47,48]</sup> Electron diffraction patterns collected on pristine and cycled LMTOF07 cathode (15 cycles) support this conclusion as shown in Figure S10 (Supporting Information). Notably, these changes are not observed in the LMTO04 and LMTOF05 compositions which maintain sloping voltage profiles after extended cycling. While the changes in the voltage profile in LMTOF06 and LMTOF07 during the first several cycles may be related to a rocksalt to a spinel-like phase transformation, it is difficult to precisely assign these features to a particular redox process. A detailed investigation of this cycling-induced phase transition and the charge compensation mechanism is important for DRX cathode design; however, such efforts would require additional advanced characterization which is beyond the scope of the present study.

**Figure 7** compares the cycling stability of LMTO04, LMTOF05, LMTOF06, and LMTOF07 DRX cathodes over 50 cycles. Corresponding voltage profiles of LMTOF samples are shown in Figure S11 (Supporting Information). Although the initial discharge capacities of LMTOF05, LMTOF06, and LMTOF07 are lower than that of LMTO04, these samples exhibit better cycling stability. After 50 cycles, LMTO04

and LMTOF05 retain 76% and 95% of their initial discharge capacity, respectively, and the capacities of LMTOF06 and LMTOF07 increase by 16% and 26%, respectively. In general, capacity retention improves with increasing Mn content. The superior cycling stability of LMTOF05, LMTOF06, and LMTOF07 is attributed to an increased contribution from Mn<sup>3+</sup>/Mn<sup>4+</sup> redox and therefore reduced dependence on oxygen redox. In LMTOF06 and LMTOF07, the increasing capacity with cycling may be due to the formation of spinel-like phases with improved Li<sup>+</sup> diffusion and hence higher active material utilization,<sup>[47,48]</sup> although we note that additional characterization studies are needed to support this conclusion. In LMTOF07, although the discharge capacity increases over the first 50 cycles, it reaches a peak value of 275 mAh g<sup>-1</sup> after 20 cycles before decreasing to 250 mAh g<sup>-1</sup> after 50 cycles, with more rapid capacity fade upon extended cycling (Figure S12, Supporting Information). Low fluorine content, oxidative decomposition of the electrolyte due to the high cutoff voltage used here (4.8 V vs Li/Li<sup>+</sup>), an unstable cathode/electrolyte interface, and manganese dissolution may all contribute to this long-term capacity fade.

The rate capability of each LMTOF cathode was also characterized by cycling the cells between 1.5 and 4.8 V at specific currents ranging from 10 to 1000 mA g<sup>-1</sup>, as shown in **Figure 8**. Overall, the discharge capacities for the LMTOF DRX samples decrease at higher rates due to higher overpotentials in the cell. In LMTOF06 and LMTOF07, the shape of the voltage profile changes with extended cycling as discussed earlier, leading to increased capacity with cycling at a given rate. In general, the rate capability improves with increasing Mn content. Increasing the specific currents from 10 mA g<sup>-1</sup> to 1000 mA g<sup>-1</sup> decreases the discharge capacities from 235, 214, 219, and 217 mAh g<sup>-1</sup> to 68, 53, 81, and 105 mAh g<sup>-1</sup> for LMTO04, LMTOF05, LMTOF06, and LMTOF07 respectively. Cycling at high rates does not induce structural damage to the active material as evidenced by the materials recovering their initial capacity when cycling at 10 mA g<sup>-1</sup> after the rate capability test.

### 3. Conclusions

This study demonstrates a sol-gel synthesis route to prepare high-performance Mn-rich, F-doped DRX cathodes. Due to homogenous atomic-level mixing of the precursors, the sol-gel route yields high-purity DRX phases at relatively low temperatures, as compared to conventional solid-state methods. Increasing the Mn content of these materials leads to improved cycling stability and rate capability. The Mn-rich compositions develop pseudo-plateaus in their voltage profiles upon cycling, likely due to the formation of a spinel-like phase, which enables an increase in the discharge capacity upon cycling. This work provides a proof of concept for a sol-gel synthesis applied to Mn-rich DRX cathodes with high capacity and good cycling stability, and the route developed here may be extended to other Co-free DRX cathodes that cover a vast compositional landscape compared to traditional Li-ion cathodes. Further optimization of the sol-gel synthesis is suggested to increase the fluorine content and fine tune the particle size and morphology of these materials.

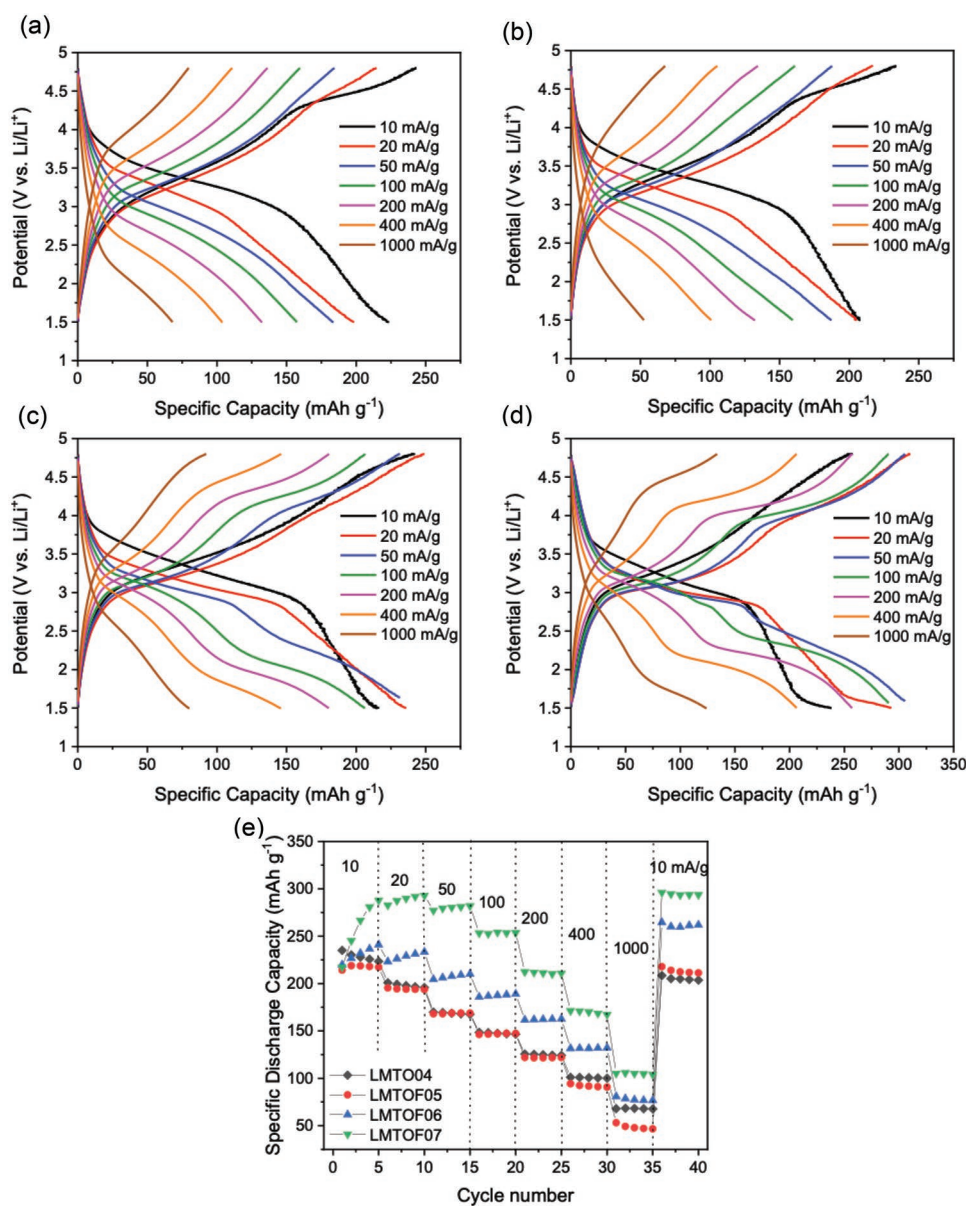


**Figure 8.** First cycle voltage profiles at varying specific currents for a) LMTO04 b) LMTOF05 c) LMTOF06 d) LMTOF07. e) Comparison of rate capability for LMTOF DRX samples. The half cells were cycled between 1.5 and 4.8 V at a specific current of 10, 20, 50, 100, 200, 400, and 1000 mA g<sup>-1</sup> for 5 cycles each.

## 4. Experimental Section

**Synthesis:** LMTOF DRX materials were synthesized using a sol-gel-based route. Product batches of 1.5 g were targeted; stoichiometric amounts of anhydrous LiNO<sub>3</sub> (Strem Chemicals, 99%), and Mn(CH<sub>3</sub>COO)<sub>2</sub>·4H<sub>2</sub>O (Sigma-Aldrich, ≥99%) were sequentially dissolved in ethanol (8 g), and then titanium isopropoxide (Alfa Aesar, 95%) was added dropwise to this solution. Glacial acetic acid (0.25 g) (Alfa Aesar, 99.7+%) was added to act as an acid catalyst, and water (0.15 g) was added to initiate the hydrolysis reaction. The solution was heated at 70 °C on a hotplate in a sand bath for 18 h to evaporate the solvent content and obtain a gel. The gel was further dried on a hot plate at 130 °C in an alumina crucible for 30 min followed by pyrolysis at 400 °C to form an intermediate oxide precursor. For LMTO04, the resulting pyrolyzed product was annealed at 1000 °C for 1 h under flowing argon.

For LMTOF05, LMTOF06, and LMTOF07, the pyrolyzed product was ball milled in a SPEX 8000 m mixer/mill with a stoichiometric amount of LiF (Alfa Aesar, 99.98%) for 1 h and then annealed at 1000 °C for 4 h under flowing argon. The heating/cooling ramp rate was ±5 °C min<sup>-1</sup>. For the ex situ phase evolution study of LMTO04 using XRD, <sup>7</sup>Li ssNMR, and electron diffraction, the sol-gel amorphous precursor was annealed at 750 °C, 900 °C, and 1000 °C for 1 h under flowing argon.

To prepare LMTO04 through a conventional solid-state route, stoichiometric amounts of Li<sub>2</sub>CO<sub>3</sub> (Sigma-Aldrich, ≥99%), TiO<sub>2</sub> (Sigma-Aldrich, ≥99.8%), Mn<sub>2</sub>O<sub>3</sub> (Sigma-Aldrich, ≥99%) were first mixed in a mortar and pestle before performing in situ XRD heating measurements as described later in this section.

**Cluster-Expansion Calculations:** To calculate the free energy of LMTO, we built a cluster-expansion Hamiltonian on the octahedral cation and anion sites of the rocksalt structure (see previous work for

details).<sup>[17]</sup> Pair interactions up to 7.1 Å, triplet interactions up to 4.0 Å, and quadruplet interactions up to 4.0 Å were included in the cluster-expansion formalism. All interactions were taken with respect to a baseline-screened electrostatic energy defined by the formal charges of the ionic species (Li<sup>+</sup>, Mn<sup>3+</sup>, Ti<sup>4+</sup>, and O<sup>2-</sup>). The effective cluster interaction (ECI) coefficients were fitted to DFT-calculated energies using an L<sub>1</sub>-regularized least-squares regression approach designed to minimize the cross-validation error. Canonical Monte Carlo simulations were carried out to obtain the internal energy of Li<sub>1.2</sub>Mn<sub>0.4</sub>Ti<sub>0.4</sub>O<sub>2</sub> as a function of temperature, from which the Gibbs free energy was calculated by integrating the heat capacity. The free energy was normalized with respect to the convex hull, which was constructed using data from density functional theory calculations made available in the Materials Project.<sup>[49]</sup>

**XRD:** Powder XRD on the as-synthesized powders was performed using a Scintag PDS 2000 diffractometer with Cu K $\alpha$  radiation ( $\lambda = 1.5406$  Å) with a nickel attenuator and a quartz zero background sample holder. Powder XRD samples were ground by hand in a mortar and pestle for 5 min. Scans had a  $2\theta$  range of 10–80° with a 0.02° step size and a 2 s integration time. Temperature-dependent XRD measurements were performed on a Malvern PANalytical X'Pert Pro MPD diffractometer (45 kV, 40 mA) equipped with Anton Paar XRK-900 reaction chamber in a  $2\theta$ - $\theta$  mode. During the XRD measurements, the reaction chamber was purged with argon to avoid unwanted sample oxidation and/or degradation. The X-ray source was Cu K $\alpha$  radiation (Cu K $\alpha_1$  with  $\lambda = 1.541$  Å and Cu K $\alpha_2$  with  $\lambda = 1.544$  Å). XRD data were collected at 100, 200, 300, 400, 500, 600, 700, 750, 800, 850, and 900 °C, where the ramp rate to each measurement temperature was 10 °C min<sup>-1</sup> and after reaching the measurement temperatures, the sample temperature was equilibrated for 1 min prior to data collection. The scan range, scan step size, and exposure time at each scan step were  $2\theta = 10$ –80°, 0.016711°, and 52.705 s, respectively. The scan parameters resulted in 61 min of total measurement time at each temperature. Phase analysis was performed for the XRD data using PANalytical HighScore Plus software,<sup>[50]</sup> and XRD-AutoAnalyzer as described in a previous publication.<sup>[51]</sup>

**Neutron Total Scattering:** Neutron total scattering data was collected at room temperature on the Nanoscale Ordered Materials Diffractometer (NOMAD, BL-1B beamline), at the Spallation Neutron Source at Oak Ridge National Laboratory.<sup>[52]</sup> 3 mm diameter quartz capillaries were used as the sample holders. The average structures were obtained via Rietveld refinement using GSAS-II software,<sup>[53]</sup> assuming a rocksalt structure with random cation ordering ( $\alpha$ -LiFeO<sub>2</sub>) as the structural model. The experimental PDF data were analyzed by least-squares “small-box” modeling using PDFgui.<sup>[54]</sup>

**ssNMR:** Solid state <sup>7</sup>Li and <sup>19</sup>F NMR spectra were acquired at  $B_0 = 2.35$  T (100 MHz for <sup>1</sup>H) using a wide bore Bruker BioSpin spectrometer equipped with a DMX 500 MHz console and a custom-made 1.3 mm single X-broadband magic angle spinning (MAS) probe tuned to <sup>7</sup>Li (38.9 MHz) or <sup>19</sup>F (94.1 MHz). Samples were loaded into 1.3 mm zirconia rotors and closed using Vespel caps in an Ar-filled glovebox. To avoid air and moisture exposure during data acquisition, the samples were spun at the magic angle (MAS) at  $\nu_R = 60$  kHz using dry nitrogen. <sup>7</sup>Li and <sup>19</sup>F chemical shifts were externally referenced against 1 M aqueous LiCl (<sup>7</sup>Li  $\delta_{iso} = 0$  ppm) and NaF (<sup>19</sup>F  $\delta_{iso} = -118.14$  ppm) solutions, respectively. Both <sup>7</sup>Li and <sup>19</sup>F MAS NMR spectra were obtained using a rotorsynchronized spin-echo sequence ( $90^\circ - \tau_R - 180^\circ - \tau_R$ ) with 90° radiofrequency (RF) pulses of 0.45  $\mu$ s and 0.30  $\mu$ s, respectively. For <sup>7</sup>Li quantitative spectra, a total of 64 transients were averaged with a recycle delay of 20 s which was enough to reach full relaxation of <sup>7</sup>Li signals. Fully relaxed <sup>19</sup>F NMR spectra were obtained with a recycle delay of 30 s and signals were averaged over 512 transients resulting in an acquisition time of 4 h 15 min per sample. To enhance the signal-to-noise ratio of <sup>19</sup>F paramagnetic signals, a much shorter recycle delay of 50 ms was used (where only paramagnetic signals are fully relaxed) which allowed a large number of transients (264 144) to be acquired in a reasonable amount of time (3 h 57 min per sample). Solid-state NMR data were processed using Bruker TopSpin 3.6.0 and spectra were fitted using DMfit software.<sup>[55]</sup>

**SEM:** SEM images of LMTOF DRX powders were collected with a Zeiss Merlin SEM using a 10 kV accelerating voltage. Some SEM images were also collected with a Hitachi TM3030Plus tabletop microscope.

**STEM/EDX Characterization:** Electron microscopy work was performed on an aberration-corrected FEI Titan 80–300™ scanning/transmission electron microscope (STEM) operated at 300 kV. TEM specimens were prepared by dispersing the cathode particles onto TEM lacey carbon grids inside an Ar-filled glovebox. The electron diffraction patterns were taken and processed using Digital Micrograph software. EDX data was collected using an Oxford X-Max EDS detector in scanning transmission mode. The quantitative EDX information was extracted using the “AZtec” software, where the overlapped peaks were deconvoluted by using the stored standard reference spectra and employing a linear least-squares procedure.

**ICP/F-ISE:** The sample compositions were determined using ICP-OES and F-ISE through Galbraith Laboratories Inc.

**Electrochemical Testing:** For cathode preparation, the active material was ball milled with SUPER C65 carbon (TIMCAL) in a 7:2 weight ratio for 1 h in a SPEX 8000 M mixer/mill. To obtain the electrode slurry, the milled mixture of active material and conductive carbon was thoroughly mixed with polyvinylidene fluoride (PVDF, Kynar) dissolved in 1-methyl-2-pyrrolidinone (NMP) (Acros Organics, 99.5%) solvent in a 7:2:1 weight ratio for 1 h using a Turbula mixer. The slurry was cast onto a carbon-coated aluminum current collector using a 200  $\mu$ m doctor blade and an automatic film coater (MTI corporation AFA-III) and dried at 90 °C under vacuum for 18 h. Electrodes (7/16-inch diameter) were punched before transferring into an Ar-filled glovebox. R2032 coin cells were assembled inside an Ar-filled glovebox using a lithium reference/counter electrode, a DRX/C/PVDF cathode, 1.2 M LiPF<sub>6</sub> in ethylene carbonate (EC)/ethyl methyl carbonate (EMC) (3:7 by weight) supporting electrolyte, and Celgard 2325 separator. Galvanostatic cycling experiments were performed at 30 °C on a MACCOR system by polarizing the working electrode between 1.5 and 4.8 V versus Li/Li<sup>+</sup> at a specific current of 10 mA g<sup>-1</sup> for the first 5 cycles and 20 mA g<sup>-1</sup> for subsequent cycles. The rate capability experiments were performed between 1.5 and 4.8 V at varying specific currents of 10, 20, 50, 100, 200, 400, and 1000 mA g<sup>-1</sup> for 5 cycles each before returning to the initial rate of 10 mA g<sup>-1</sup>.

For the ex-situ electron diffraction measurements to observe the cycling-induced phase transition, the LMTOF07 cathode was cycled in a half cell for 15 cycles at a specific current of 10 mA g<sup>-1</sup> for the first 5 cycles and 20 mA g<sup>-1</sup> for subsequent cycles and extracted from the cell in the charged state. The cathode was dried under vacuum at room temperature overnight.

## Supporting Information

Supporting Information is available from the Wiley Online Library or from the author.

## Acknowledgements

S.P. and D.D. contributed equally to this work. Research conducted at Oak Ridge National Laboratory, managed by UT Battelle, LLC, for the U.S. Department of Energy (DOE) was sponsored by the Vehicle Technologies Office (VTO) under the Office of Energy Efficiency and Renewable Energy (EERE). Neutron scattering experiments were performed on the NOMAD beamline (BL-1B) at the Spallation Neutron Source, a DOE Office of Science User Facility operated by Oak Ridge National Laboratory. Some X-ray diffraction and scanning electron microscopy measurements were conducted at the Center for Nanophase Materials Sciences (CNMS), which is a DOE Office of Science User Facility. Ab-initio calculations were performed with support from the Assistant Secretary for Energy Efficiency and Renewable Energy, Vehicle Technologies Office, under the Applied Battery Materials Program, of the U.S. Department of Energy (DOE)

under contract no. DE-AC02-05CH11231. The NMR experimental work reported here was supported by the Assistant Secretary for Energy Efficiency and Renewable Energy, Office of Vehicle Technologies of the U.S. Department of Energy under Contract No. DE-AC02-05CH11231 and made use of the shared facilities of the UCSB MRSEC (NSF DMR 1720256), a member of the Material Research Facilities Network. The STEM/EDX experimental work reported here was performed under the support of the Assistant Secretary for Energy Efficiency and Renewable Energy, Vehicle Technologies Office, of the U.S. Department of Energy under Contract No. DE-LC-000L053 under the program of Next Generation Cathode and made use of the William R. Wiley Environmental Molecular Sciences Laboratory, a national scientific user facility sponsored by U.S. Department of Energy, Office of Biological and Environmental Research and located at PNNL. PNNL is operated by Battelle for the U.S. Department of Energy under Contract DE-AC05-76RLO1830. V.C.W. was supported by the National Science Foundation Graduate Research Fellowship under Grant No. DGE 1650114. N.J.S. was supported by the National Science Foundation Graduate Research Fellowship under grant No. DGE 1752814.

This manuscript has been authored in part by UT-Battelle, LLC, under contract DE-AC05-00OR22725 with the US Department of Energy (DOE). The publisher, by accepting the article for publication, acknowledges that the US government retains a nonexclusive, paid-up, irrevocable, worldwide license to publish or reproduce the published form of this manuscript, or allow others to do so, for US government purposes. DOE will provide public access to these results of federally sponsored research in accordance with the DOE Public Access Plan.

## Conflict of Interest

The authors declare no conflict of interest.

## Data Availability Statement

The data that support the findings of this study are available from the corresponding author upon reasonable request.

## Keywords

cation disordered rocksalts, lithium-ion battery cathodes, manganese-rich, sol-gel, synthesis

Received: September 29, 2022

Revised: November 17, 2022

Published online:

- [1] M. Li, J. Lu, Z. Chen, K. Amine, *Adv. Mater.* **2018**, *30*, 1800561.  
 [2] A. Manthiram, *Nat. Commun.* **2020**, *11*, 1550.  
 [3] J. Xie, Y.-C. Lu, *Nat. Commun.* **2020**, *11*, 2499.  
 [4] N. Nitta, F. Wu, J. T. Lee, G. Yushin, *Mater. Today* **2015**, *18*, 252.  
 [5] M. S. Whittingham, *Chem. Rev.* **2004**, *104*, 4271.  
 [6] E. A. Olivetti, G. Ceder, G. G. Gaustad, X. Fu, *Joule* **2017**, *1*, 229.  
 [7] K. Turcheniuk, D. Bondarev, V. Singhal, G. Yushin, *Nature* **2018**, *559*, 467.  
 [8] J. Lee, A. Urban, X. Li, D. Su, G. Hautier, G. Ceder, *Science* **2014**, *343*, 519.  
 [9] A. Urban, J. Lee, G. Ceder, *Adv. Energy Mater.* **2014**, *10*.  
 [10] R. J. Clément, Z. Lun, G. Ceder, *Energy Environ. Sci.* **2020**, *13*, 345.  
 [11] D. Chen, J. Ahn, G. Chen, *ACS Energy Lett.* **2021**, *6*, 1358.

- [12] J. Lee, D. A. Kitchaev, D.-H. Kwon, C.-W. Lee, J. K. Papp, Y.-S. Liu, Z. Lun, R. J. Clément, T. Shi, B. D. McCloskey, J. Guo, M. Balasubramanian, G. Ceder, *Nature* **2018**, *556*, 185.  
 [13] N. Yabuuchi, M. Nakayama, M. Takeuchi, S. Komaba, Y. Hashimoto, T. Mukai, H. Shiiba, K. Sato, Y. Kobayashi, A. Nakao, M. Yonemura, K. Yamanaka, K. Mitsuhashi, T. Ohta, *Nat. Commun.* **2016**, *7*, 13814.  
 [14] D.-H. Seo, J. Lee, A. Urban, R. Malik, S. Kang, G. Ceder, *Nat. Chem.* **2016**, *8*, 692.  
 [15] E. Zhao, Q. Li, F. Meng, J. Liu, J. Wang, L. He, Z. Jiang, Q. Zhang, X. Yu, L. Gu, W. Yang, H. Li, F. Wang, X. Huang, *Angew. Chem., Int. Ed.* **2019**, *58*, 4323.  
 [16] W. D. Richards, S. T. Dacek, D. A. Kitchaev, G. Ceder, *Adv. Energy Mater.* **2018**, *8*, 1701533.  
 [17] B. Ouyang, N. Artrith, Z. Lun, Z. Jadidi, D. A. Kitchaev, H. Ji, A. Urban, G. Ceder, *Adv. Energy Mater.* **2020**, *10*, 1903240.  
 [18] Z. Lun, B. Ouyang, D. A. Kitchaev, R. J. Clément, J. K. Papp, M. Balasubramanian, Y. Tian, T. Shi, B. D. McCloskey, J. Lee, G. Ceder, *Adv. Energy Mater.* **2019**, *9*, 1802959.  
 [19] Z. Jadidi, T. Chen, P. Xiao, A. Urban, G. Ceder, *J. Mater. Chem. A* **2020**, *8*, 19965.  
 [20] J. Ahn, D. Chen, G. Chen, *Adv. Energy Mater.* **2020**, *10*, 2001671.  
 [21] J. Lee, J. K. Papp, R. J. Clément, S. Sallis, D.-H. Kwon, T. Shi, W. Yang, B. D. McCloskey, G. Ceder, *Nat. Commun.* **2017**, *8*, 981.  
 [22] Y. Yue, N. Li, L. Li, E. E. Foley, Y. Fu, V. S. Battaglia, R. J. Clément, C. Wang, W. Tong, *Chem. Mater.* **2020**, *32*, 4490.  
 [23] D. Chen, J. Ahn, E. Self, J. Nanda, G. Chen, *J. Mater. Chem. A* **2021**, *9*, 7826.  
 [24] R. Chen, S. Ren, M. Knapp, D. Wang, R. Witter, M. Fichtner, H. Hahn, *Adv. Energy Mater.* **2015**, *5*, 1401814.  
 [25] Z. Lun, B. Ouyang, Z. Cai, R. J. Clément, D.-H. Kwon, J. Huang, J. K. Papp, M. Balasubramanian, Y. Tian, B. D. McCloskey, H. Ji, H. Kim, D. A. Kitchaev, G. Ceder, *Chem* **2020**, *6*, 153.  
 [26] R. A. House, L. Jin, U. Maitra, K. Tsuruta, J. W. Somerville, D. P. Förstermann, F. Massel, L. Duda, M. R. Roberts, P. G. Bruce, *Energy Environ. Sci.* **2018**, *11*, 926.  
 [27] N. J. Szymanski, Y. Zeng, T. Bennett, S. Patil, J. K. Keum, E. C. Self, J. Bai, Z. Cai, R. Giovine, B. Ouyang, F. Wang, C. J. Bartel, R. J. Clément, W. Tong, J. Nanda, G. Ceder, *Chem. Mater.* **2022**, *34*, 7015.  
 [28] R. Dominko, C. V.-A. Garrido, M. Bele, M. Kuezma, I. Arcon, M. Gaberscek, *J. Power Sources* **2011**, *196*, 6856.  
 [29] E. Zhao, L. He, B. Wang, X. Li, J. Zhang, Y. Wu, J. Chen, S. Zhang, T. Liang, Y. Chen, X. Yu, H. Li, L. Chen, X. Huang, H. Chen, F. Wang, *Energy Storage Mater.* **2019**, *16*, 354.  
 [30] D. A. Kitchaev, Z. Lun, W. D. Richards, H. Ji, R. J. Clément, M. Balasubramanian, D.-H. Kwon, K. Dai, J. K. Papp, T. Lei, B. D. McCloskey, W. Yang, J. Lee, G. Ceder, *Energy Environ. Sci.* **2018**, *11*, 2159.  
 [31] A. E. Danks, S. R. Hall, Z. Schnepf, *Mater. Horiz.* **2016**, *3*, 91.  
 [32] Y.-K. Sun, I.-H. Oh, S.-A. Hong, *J. Mater. Sci.* **1996**, *31*, 3617.  
 [33] Y.-K. Sun, I.-H. Oh, *J. Mater. Sci. Lett.* **1997**, *16*, 30.  
 [34] Y.-K. Sun, I.-H. Oh, K. Y. Kim, *Ind. Eng. Chem. Res.* **1997**, *36*, 4839.  
 [35] X. Ma, H. He, Y. Sun, Y. Zhang, *J. Mater. Sci.: Mater. Electron.* **2017**, *28*, 16665.  
 [36] D.-q. Liao, C.-y. Xia, X.-m. Xi, C.-x. Zhou, K.-s. Xiao, X.-q. Chen, S.-b. Qin, *J. Sol-Gel Sci. Technol.* **2016**, *78*, 403.  
 [37] C. P. Grey, N. Dupré, *Chem. Rev.* **2004**, *104*, 4493.  
 [38] H. Ji, A. Urban, D. A. Kitchaev, D.-H. Kwon, N. Artrith, C. Ophus, W. Huang, Z. Cai, T. Shi, J. C. Kim, H. Kim, G. Ceder, *Nat. Commun.* **2019**, *10*, 592.  
 [39] Z. Lun, B. Ouyang, D.-H. Kwon, Y. Ha, E. E. Foley, T.-Y. Huang, Z. Cai, H. Kim, M. Balasubramanian, Y. Sun, J. Huang, Y. Tian, H. Kim, B. D. McCloskey, W. Yang, R. J. Clément, H. Ji, G. Ceder, *Nat. Mater.* **2021**, *20*, 214.  
 [40] R. J. Clément, D. Kitchaev, J. Lee, G. Ceder, *Chem. Mater.* **2018**, *30*, 6945.

- [41] M. A. Jones, P. J. Reeves, I. D. Seymour, M. J. Cliffe, S. E. Dutton, C. P. Grey, *Chem. Commun.* **2019**, 55, 9027.
- [42] W. H. Kan, B. Deng, Y. Xu, A. K. Shukla, T. Bo, S. Zhang, J. Liu, P. Pianetta, B.-T. Wang, Y. Liu, G. Chen, *Chem* **2018**, 4, 2108.
- [43] Z. Cai, Y.-Q. Zhang, Z. Lun, B. Ouyang, L. C. Gallington, Y. Sun, H.-M. Hau, Y. Chen, M. C. Scott, G. Ceder, *Adv. Energy Mater.* n/a, 2103923.
- [44] W. H. Kan, D. Chen, J. K. Papp, A. K. Shukla, A. Huq, C. M. Brown, B. D. McCloskey, G. Chen, *Chem. Mater.* **2018**, 30, 1655.
- [45] M. J. Crafton, Y. Yue, T. Y. Huang, W. Tong, B. D. McCloskey, *Adv. Energy Mater.* **2020**, 10, 2001500.
- [46] D. Chen, J. Wu, J. K. Papp, B. D. McCloskey, W. Yang, G. Chen, *Small* **2020**, 16, 2000656.
- [47] L. Li, Z. Lun, D. Chen, Y. Yue, W. Tong, G. Chen, G. Ceder, C. Wang, *Adv. Funct. Mater.* **2021**, 31, 2101888.
- [48] J. Ahn, Y. Ha, R. Satish, R. Giovine, L. Li, J. Liu, C. Wang, R. J. Clement, R. Kostecki, W. Yang, G. Chen, *Adv. Energy Mater.* n/a, 2200426.
- [49] A. Jain, S. P. Ong, G. Hautier, W. Chen, W. D. Richards, S. Dacek, S. Cholia, D. Gunter, D. Skinner, G. Ceder, K. A. Persson, *APL Mater.* **2013**, 1, 011002.
- [50] T. Degen, M. Sadki, E. Bron, U. König, G. Nénert, *Powder Diff.* **2014**, 29, S13.
- [51] N. J. Szymanski, C. J. Bartel, Y. Zeng, Q. Tu, G. Ceder, *Chem. Mater.* **2021**, 33, 4204.
- [52] J. Neufeind, M. Feygenson, J. Carruth, R. Hoffmann, K. K. Chipley, *Nucl. Instrum. Methods Phys. Res. B: Beam Interact. Mater. At.* **2012**, 287, 68.
- [53] B. H. Toby, R. B. Von Dreele, *J. Appl. Crystallogr.* **2013**, 46, 544.
- [54] C. L. Farrow, P. Juhas, J. W. Liu, D. Bryndin, E. S. Božin, J. Bloch, T. Proffen, S. J. L. Billinge, *J. Phys.: Condens. Matter* **2007**, 19, 335219.
- [55] D. Massiot, F. Fayon, M. Capron, I. King, S. L. Calvé, B. Alonso, J.-O. Durand, B. Bujoli, Z. Gan, G. Hoatson, *Magn. Reson. Chem.* **2002**, 40, 70.